Journal of Advanced Research in Numerical Heat Transfer

Journal homepage:
https://semarakilmu.com.my/journals/index.php/arnht/index
ISSN: 2735-0142

# Numerical Simulation of Surface Pressure and Temperature Distribution Along a Cone at Supersonic Mach Numbers Using CFD

Javed Shoukat Shaikh[1], Shamitha Shetty[2], Khizar Ahmed Pathan[3], Sher Afghan Khan[3,*], Qazi Fasihuddin[5], Krishna Kumar[6]

[1] Department of Mathematics, School of Computational Sciences, Faculty of Science and Technology, JSPM University, Pune-412207, Maharashtra, India
[2] Department of Mathematics, Nitte Meenakshi Institute of Technology Bangalore, Affiliated to VTU, 560064, India
[3] Department of Mechanical Engineering, CSMSS Chh. Shahu College of Engineering, Aurangabad, 431011, India
[4] Department of Mechanical and Aerospace Engineering, Faculty of Engineering, IIUM, Gombak Campus, Kuala Lumpur, Malaysia
[5] School of Electrical and communication Sciences, Faculty of Science and Technology, JSPM University, Pune-412207,Maharashtra, India
[6] Department of Applied Science and Humanities , MIT School of Computing, MIT-ADT University, Pune-412201, Maharashtra, India

**ARTICLE INFO**

***Article history:***
Received 5 September 2024
Received in revised form 1 October 2024
Accepted 9 November 2024
Available online 15 December 2024

***Keywords:***
Mach number; Supersonic flow; semi-cone angle; CFD

**ABSTRACT**

The primary focus of this study is to use numerical simulations to analyze the static temperature and surface pressure distribution along the slant length of a cone at different Mach numbers and a range of semi-cone angles. Computational fluid dynamics (CFD) analysis numerically simulates temperature and surface pressure distribution. This research considers parameters such as supersonic Mach numbers, semi-cone angles, and different locations along the slant length of a cone. The study examines Mach numbers of 1.5, 2.0, 2.5, 3.0, 3.5, 4.0, 4.5, and 5.0, along with cone angles ranging from 3° to 21°. The static temperature and pressure (P/Pa) results are measured at different locations (x/L) along the slant length of the cone, ranging from 0.1 to 1. The results for static temperature and pressure distribution obtained by CFD analysis are compared with results obtained by regression model at various Mach numbers and constant semi-cone angle (θ) = 12°. The results from the CFD analysis and the findings of the regression methodology are in agreement. This study found that the Mach number, semi-cone angle, and the various locations along the cone's slant length significantly impact the variation of static temperature and surface pressure distribution. As the Mach number and the semi-cone angle increase, the temperature and pressure distribution along the slant length of the cone also increase.

## 1. Introduction

The advent of military jets such as the space shuttle fuels the growing demand for design expertise in delta wing shapes. To ensure these aircraft meet performance benchmarks, assessing their aerodynamic load and stability is crucial. Numerous studies have underscored the significance

* *Corresponding author.*
*E-mail address: sakhan@iium.edu.my (Sher Afghan Khan)*

https://doi.org/10.37934/arnht.28.1.126

of accurately forecasting performance at angles of attack during re-entry. Aerospace vehicles face shock waves during descent when traveling at velocities. These shock waves can either detach from or adhere to the leading edges of the wings. Opting for the scenario concerning shock attachment is often favored to enhance the lift-to-drag ratio. In this situation, the surfaces of the wings do not interact, enabling independent resolution of challenges. Consequently, the flow field on the surface, whether steady or unsteady, can be initially examined. Furthermore, considering vortex sheet formation is vital. The importance of flow separation at angles is frequently overlooked. To obtain solutions, researchers employed a combination of supersonic and hypersonic techniques. Earlier methods grounded in the hypersonic small disturbance theory were limited to situations where the outer region exceeded the center region marked by the Mach cone.

Hui later expanded on this idea to create a more encompassing supersonic hypersonic theory that removes these previous limitations. Hui's findings in the region derived from this approach are considered to be a deviation from the standard wedge flow. Interestingly, insights drawn from theory closely resemble results obtained from simulations. The concept of hypersonic similarity originates from the work of Tsien [1], who explored the equations of motion in two-dimensional and axis-symmetric cases. Hayes [2] expanded on Tsien's work by introducing the concept of hypersonic similitude, highlighting the critical role of similarity parameters in predicting aerodynamic characteristics. Sychev's [3] approach to hypersonic similarity with large incidence is relevant for wings with a minimal span. In supersonic and hypersonic airflow with shock waves, Pike [4] and Hui [5] explain the stability of delta wings. Carrier [6] and Hui [7] presented solutions for two-dimensional flow involving an oscillating wedge and an oscillating flat plate. Their findings are relevant across all supersonic Mach numbers (M) and wedge angles accompanied by a shock wave.

The study by Orlik-Ruckemann [8] emphasized the importance of stability in situations where the angle of incidence is high, such as during re-entry or maneuvering. In aerodynamics, it is crucial to uphold control and stability across various flight conditions, including steep angles of attack or incidence, to ensure that an aircraft or spacecraft exhibits dynamic stability. Lui and Hui [9] expanded on the theory introduced by Hui and Hemdan [10] by integrating a delta wing with a connected shock wave. Lighthill [11] introduced a theoretical framework called "Piston Theory" and integrated a new variable, δ, into it. Ghosh [12] has developed impactful advanced 2-D hypersonic similitude and piston theory. Lighthill [11] and Miles [13] provided insights into oscillating aerofoils at high Mach numbers, further revealing the complex interactions between shock waves and body surfaces.

The investigation into the oscillating wedge and the concept of hypersonic similitude at high angles of incidence was conducted by Ghosh and Mistry [14]. Ghosh [15] also showcased the similitude of quasi wedges and quasi cones in hypersonic flow conditions with large deflection. In their research, Khan *et al.,* [16] delved into the flow characteristics of wedges through CFD (Computational Fluid Dynamics) simulations. Meanwhile, Musavir *et al.,* [17] conducted both computational and analytical assessments of aerodynamic derivatives for delta wings at hypersonic speeds. Kalimuthu *et al.,* [18] demonstrated that adding a spike to a blunt-nosed body significantly impacts the flow field and aerodynamic coefficients during hypersonic flight. Pathan *et al.,* [19] showcased how boat tail helmet designs can reduce drag. Shaikh *et al.*, [20-22] conducted computational analyses specifically targeting surface pressure distribution over 2D wedge and slant length of cones in high-speed flows. Azami *et al.,* [23] investigated wall pressure distribution and the effects of microjets, while Pathan *et al.,* [24] utilized CFD analysis to study base pressure fluctuations in internal and external flows.

Khan *et al.,* [25] and Pathan *et al.,* [26-30] examined and employed various approaches to assess base pressure. In their study of suddenly expanded flow, Pathan *et al.,* [26-30] concentrated on improving duct length, whereas Pratibha *et al.,* [31,32] compared the effectiveness of linear

regression and regression trees in different situations to see how they can be applied. The efficiency of logistic regression and tree algorithms in categorizing categorical outcomes is assessed, with a focus on the strengths of each method. Aqilah *et al.,* [33] further corroborate the viability of passive control mechanisms. They also indicate that the intricacies of high-speed aerodynamics warrant further exploration. Fiqri *et al,.* [34] illustrate the vast array of geometric modifications that can be employed in passive control applications .

Pathan *et al.,* [35] highlight effective geometric optimization's multifaceted advantages in aerospace engineering. An investigation by Shaikh *et al.,* [36,37] sought to realize flow uniformity while minimizing pressure drop across the monolith. The implications derived from their findings underscore the significance of uniform flow distribution. Kumar and Kalita [38,39] formulated the transformation free ψ-v scheme for Navier–Stokes equations and two-dimensional laminar flow past bluff bodies on compact nonuniform grids. Vortex dynamics of accelerated flow past a mounted wedge. Kalita and Kumar [40] studied the complex fluid flow problem simulation involving vortex dynamics of accelerated flow past a mounted wedge. Akbar *et al.,* [41-43] studied the enhancement of heat transfer, thermal and concentration storage analysis in cone-disk, and simulation of hybrid boiling nanofluid flow.

This research aims to investigate the surface pressure distribution along the slant length of the cone. The pressure assessment uses CFD simulations in ANSYS workbench considering varying semi-cone angles (θ) and Mach numbers. The findings from the CFD analysis and parametric study serve as the basis for this examination. The Mach numbers studied span from 1.5 to 5 while the semi-cone angles range between 3° and 21°. Moreover, the slant length of the cone is examined at positions varying from 0.1 to 1. Figure 1 depicts the shape of the cone.

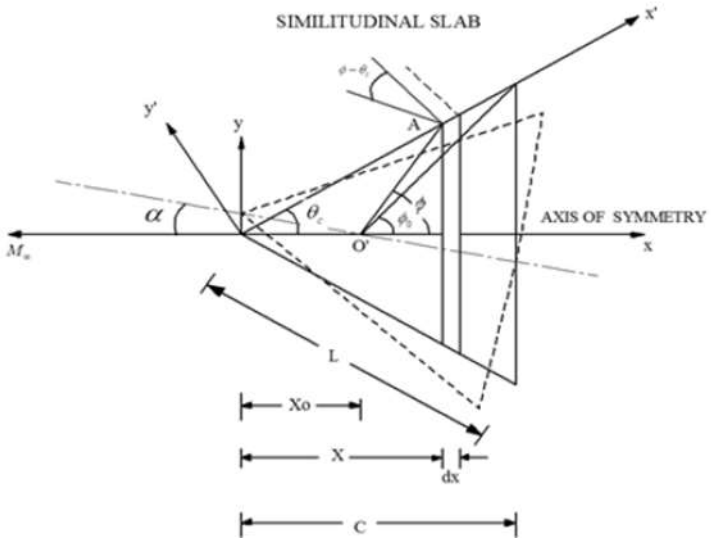


**Fig. 1.** Cone Geometry

At zero incidence, in the case of bow-attached shock, Eq. (1) provides the pressure ratio at the nose of the steady cone obtained by Ghosh's [15] as,

$$\frac{P_a}{P_\infty} = 1 + \gamma M_P^2 \left(1 + \frac{1}{4}\varepsilon\right) \tag{1}$$

where,

$$\varepsilon = \frac{2 + (\gamma - 1)M_P^2}{2 + (\gamma + 1)M_P^2} \tag{2}$$

here $\varepsilon$ is the density ratio, $P_a$ is pressure on the surface of the cone (body) at zero incidences, $M_P$ is the piston Mach number of the equivalent piston.

The piston Mach number is given by,

$$M_P = M_\infty \sin\theta_c \tag{3}$$

here, $\theta_c$ represents the semi-angle of the cone.

In the scenario involving an oscillating cone, we followed Ghosh [15], where the cone's surface is positioned perpendicular to the similitude slab at a distance $x_1$ from the apex. The cone is characterized by non-slender properties exhibiting low frequency and amplitude oscillations in pitch. Consequently, we assume the flow is quasi-steady and exhibits quasi-axisymmetric behavior. Given that the cone moves into the slab at a Mach number, the piston's relative Mach number is denoted as $M_P$. For the quasi-cone problem with wide deflection similitude, it is determined that the pressure ratio equation holds when the Mach number behind the shock is equal to or exceeds 2.5. This limitation is essential in the presence of Mach waves within the flow. Therefore, it is crucial to uphold Ghosh's [15] similitude in the context of the oscillating cone scenario. This study examines how the surface pressure distribution changes along the cone's slant length. Different flow parameters are applied to the cone to numerically simulate the surface pressure using Computational Fluid Dynamics (CFD) analysis to achieve this. The numerical results obtained for the surface pressure of the cone are based on Mach Numbers 1.5, 2.0, 2.5, 3.0, 3.5, 4.0, 4.5, and 5.0 and semi angles of the cone ranging from 3° to 21°.

## 2. Methodology

### *2.1 CFD Analysis*

The study uses Computational Fluid Dynamics (CFD) techniques using ANSYS Workbench and Fluent software under an Academic license. ANSYS Workbench handles tasks such as Meshing and modeling, while ANSYS Fluent is used for the analysis and post-processing phases. To ensure precise numerical results, a structured mesh is implemented. The analysis considers Mach numbers 1.5,2.0,2.5,3.0,3.5,4.0,4.5, and 5.0, along with semi-cone angles varying from 3° to 21°. All relevant parameters are considered during the CFD analysis of weak solutions with an accompanying shock wave. For the CFD analysis, air is treated as a perfect gas.

#### *2.1.1 Modeling*

The various cone angle shapes are generated using ANSYS Design Modeler, as illustrated in Figure 2. This figure showcases the forms of the cone and its surrounding enclosure. Different cone angles ranging from 3° to 21° are considered for all designs while maintaining a constant length (L) of 10 for each setup. The enclosure is designed explicitly for analysis purposes with lengths of five times (L) on the top and bottom sides, three times (L) on the front side, and five times (L) on the backside. Figure 2 indicates the inlet and outlet on the front and back edges.

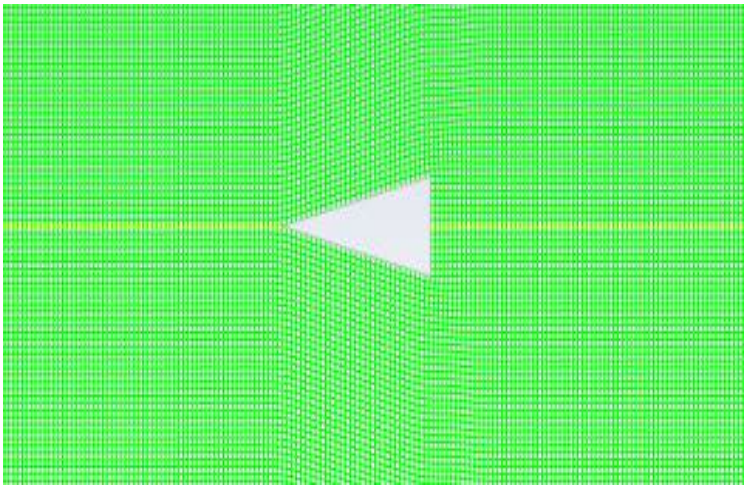

**Fig. 2.** Sketch of enclosure for CFD analysis and cone geometry

### *2.1.2 Meshing*

Before proceeding with the meshing process, the grid independence test was conducted to determine the optimal mesh size. This test used mesh sizes ranging from 1 mm to 15 mm for a semi-cone angle of 12° and a Mach number of 3. The findings of the grid independence test are presented in Figure 3. The results indicate that the outcomes remain consistent with a mesh element size of 2 mm, suggesting that this size can be used for future CFD analyses. However, a mesh element size of 1 mm is chosen to enhance accuracy in subsequent CFD evaluations. Table 1 exhibits the number of nodes and elements for the mesh sizes ranging from 15mm to 1mm.

In Figure 4(a), we can see the 2D axisymmetric mesh model and take a closer look at the cone shape in Figure 4(b). The Hexahedral dominant mesh approach is used for the overall meshing process.

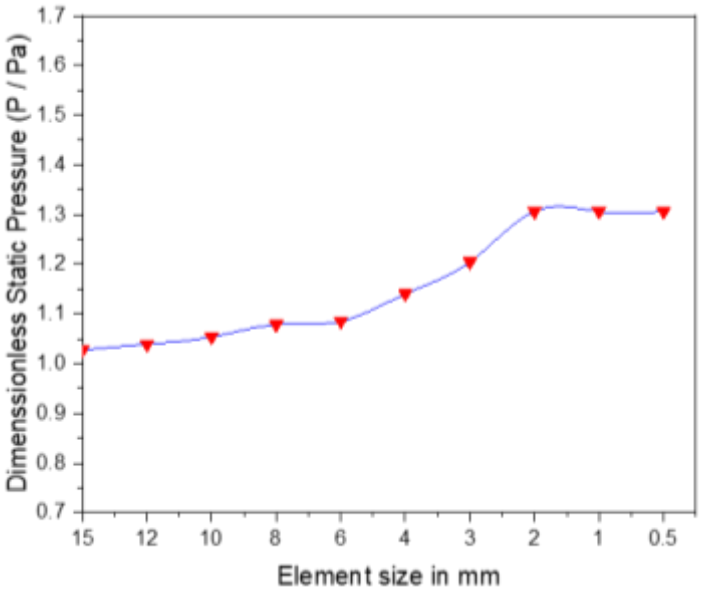


**Fig. 3.** Grid independence test

**Table 1**
Grid independence test: Number of mesh elements with various element sizes

| Mesh Element Size in (mm) | Mesh Nodes | Mesh Elements | $P/P_a$ |
|---|---|---|---|
| 15 | 1723 | 1633 | 1.02770099 |
| 12 | 2618 | 2508 | 1.03925435 |
| 10 | 3727 | 3596 | 1.05408116 |
| 8 | 5774 | 5611 | 1.07859667 |
| 6 | 10291 | 10071 | 1.0855974 |
| 4 | 22860 | 22529 | 1.14063137 |
| 3 | 40105 | 39675 | 1.20520673 |
| 2 | 90422 | 89771 | 1.30675733 |
| 1 | 360295 | 358992 | 1.30677325 |

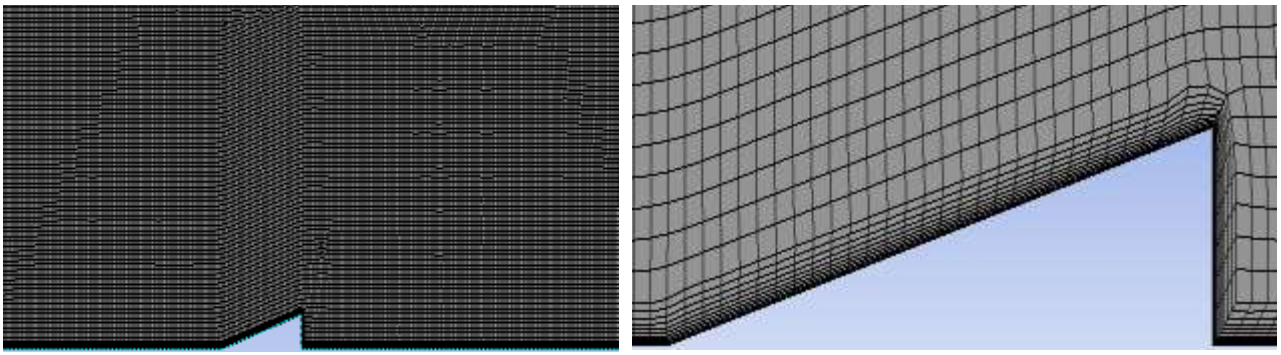

(a) (b)

**Fig. 4.** 2D meshed geometry for θ=12° (a) Complete Geometry (b) Enlarged view of cone

### *2.1.3 CFD analysis*

The CFD study entails a thorough exploration of parameter combinations. The solution is initialized after setting the boundary conditions and undergoes at least 10000 iterations. In certain instances, convergence is achieved within just 1000 iterations. This analysis employs the commonly used k-epsilon turbulence model and two additional transport equations to capture the flow attributes accurately. The inlet and pressure outlet are specified to establish the inflow and outflow boundary conditions, respectively. The inlet velocity is determined based on the Mach number, while the outlet pressure is set at atmospheric pressure. The SIMPLE method is utilized during the analysis, and the density-based problem solver is chosen due to the high-speed and compressible flow.

### *2.2 Results of Temperature Contours*

The temperature contours for Mach number (M = 3) are illustrated in Figures 5 a-c showcasing a cone with a semi-cone angle of 12°. The contour plot vividly illustrates a temperature distribution within a flow field that envelops a cone. The leading edge of the cone undergoes considerable heating, primarily because of the interaction between the flow and the object. However, the downstream regions exhibit a marked decrease in temperature; this phenomenon occurs as the flow migrates away from the cone. Although one might expect a gradual transition, the temperature decline is surprisingly abrupt, thus highlighting the complex dynamics in such flow fields.

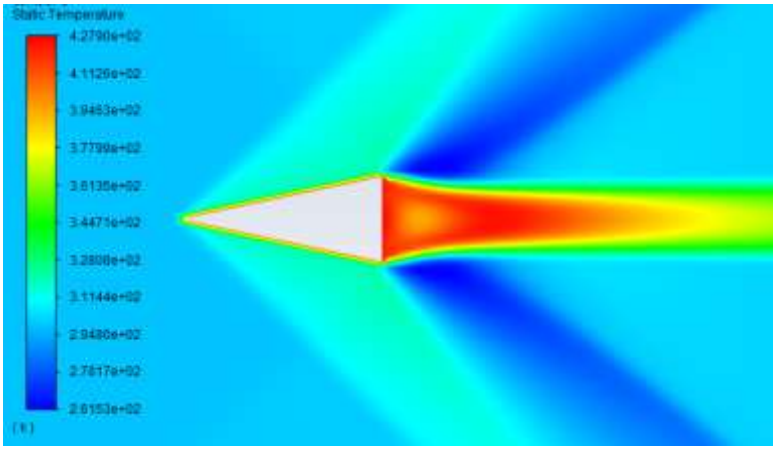


(a)

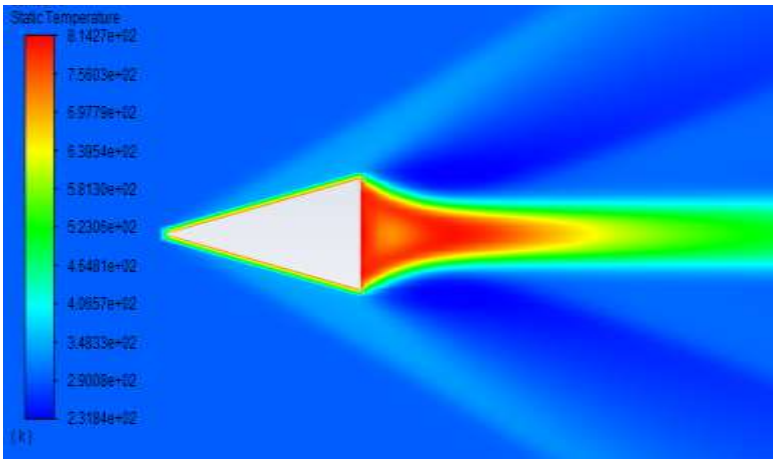


(b)

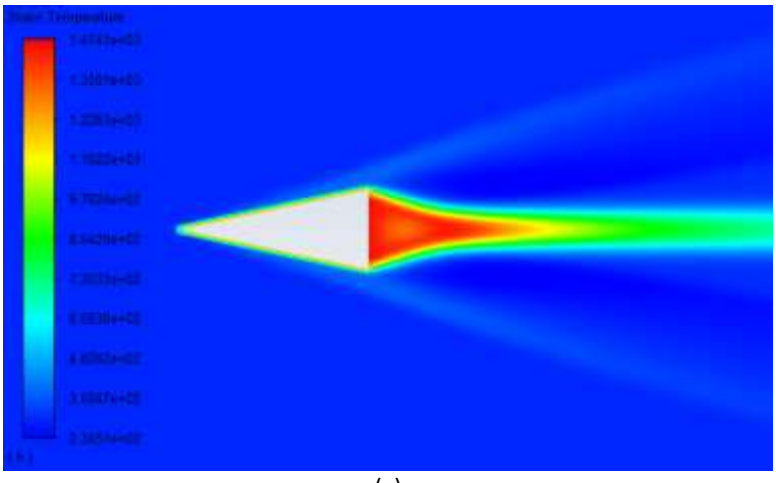

(c)

**Fig. 5.** Contour of static temperature (a) for Mach number (M) = 1.5 at a semi-cone angle (θ) = 12°, (b) for Mach number (M) = 3 at a semi-cone angle (θ) = 12°, (c) for Mach number (M) = 4.5 at a semi-cone angle (θ) = 12°

### *2.3 Results of Pressure Contours*

The pressure contours at Mach numbers (M=3) are illustrated in Figures 6 a-c, showcasing a cone with a semi-cone angle of 12°. This plot visualizes the static pressure distribution around a triangular

body subjected to high-speed flow. The significant pressure increase near the leading edge indicates the presence of a shock wave, while the low-pressure regions behind the object represent flow separation and wake formation.

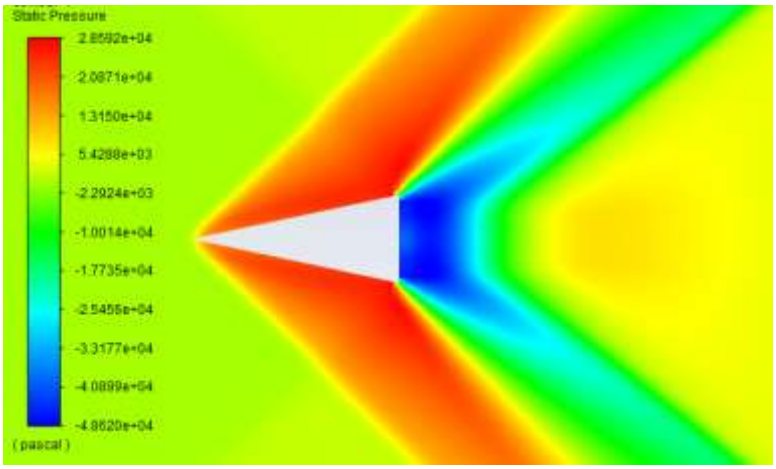


(a)

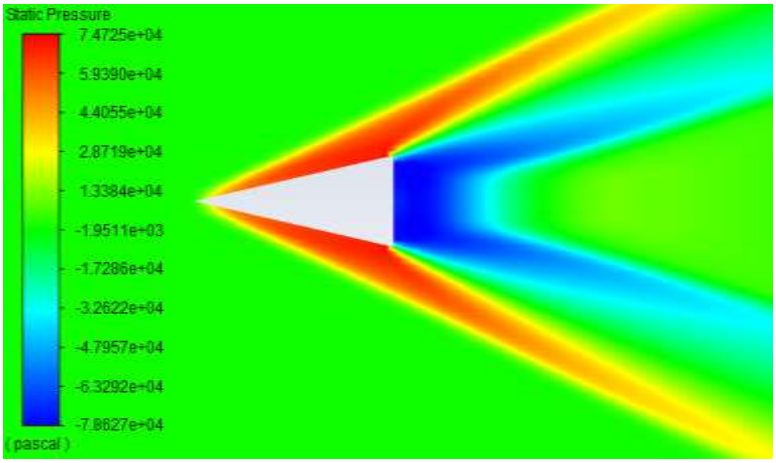


(b)

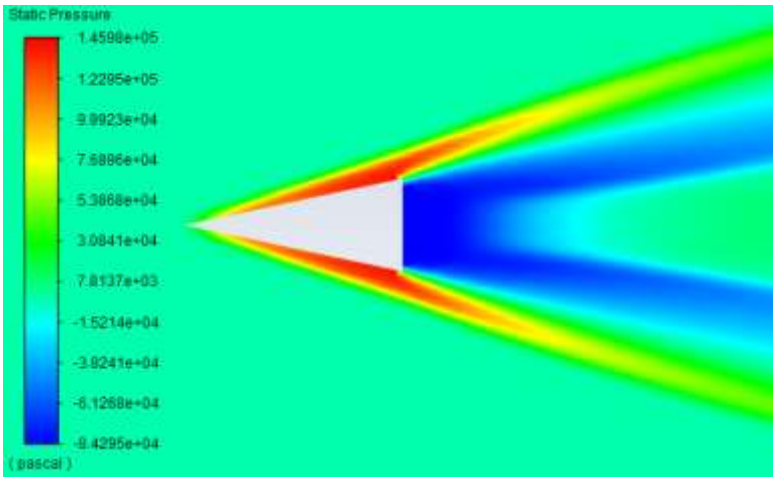


(c)

**Fig. 6.** Contour of static pressure (a) for Mach number (M) = 1.5 at a semi-cone angle (θ) = 12°, (b) for Mach number (M) = 3 at a semi-cone angle (θ) = 12°, (c) for Mach number (M) = 4.5 at a semi-cone angle (θ) = 12°

## 3. Results for Temperature

### *3.1 Main Effects Mach Number Plots for Static Temperature*

The main effects plot shown in Figure 7 showcases the relationship between the Mach Number (M) and the average static temperature. It shows a positive, non-linear relationship between the Mach number (M) and the static temperature. The figure reveals that with the rise in Mach number from 1.5 to 2.5, temperature steadily increases. However, when the Mach number exceeds 3.0, the change becomes more pronounced, exhibiting a curve that indicates a surge in static temperature.

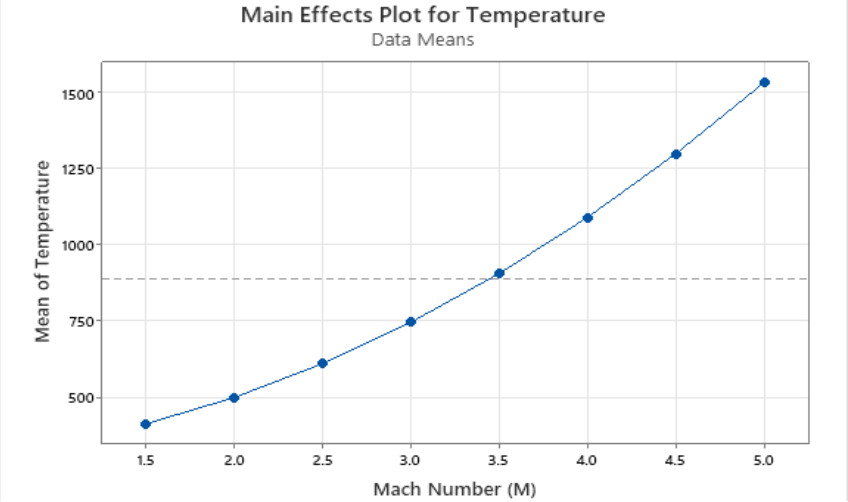


**Fig. 7.** Effect of Mach numbers on the static temperature along the slant length of the cone

### *3.2 Main Effects Semi-Cone Angle Plots for Dimensionless Static Temperature*

The main effects plot shown in Figure 8 reveals the relationship between the Mach Number (M) and the average static temperature. The plot indicates a positive linear relationship between the semi-cone angle (θ) and the mean temperature. The plot demonstrates that increasing the semi-cone angle causes a temperature rise. This indicates that along the slant length of the cone, there is a strong dependency on temperature on the semi-cone angle of the cone.

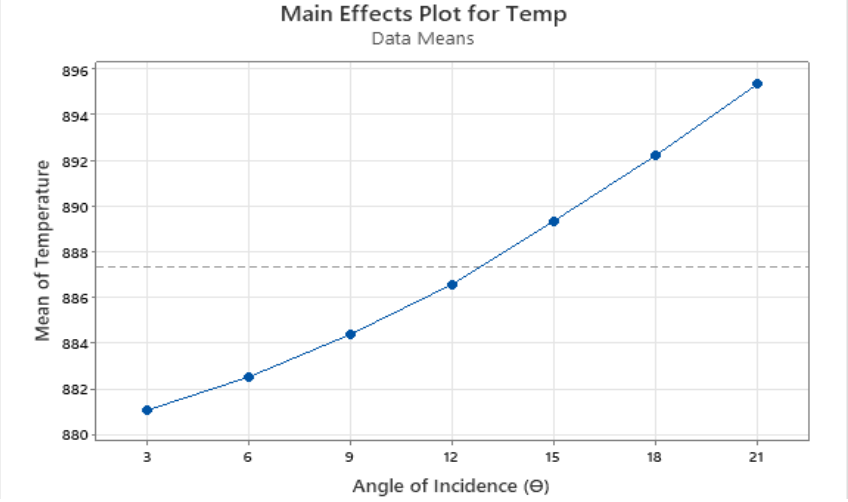


**Fig. 8.** Effect of semi-cone angle on the static temperature along the slant length of the cone

### *3.3 Main Effects of Location along Slant Length of the Cone for Dimensionless Static Temperature*

The main effects plot shown in Figure 9 displays the relationship between the location and the average static temperature. The plot indicates a rapid increase in temperature up to location 0.3 along the slant length. After the initial increase, the temperature decreases from location 0.3 to 1.0 along the slant length.

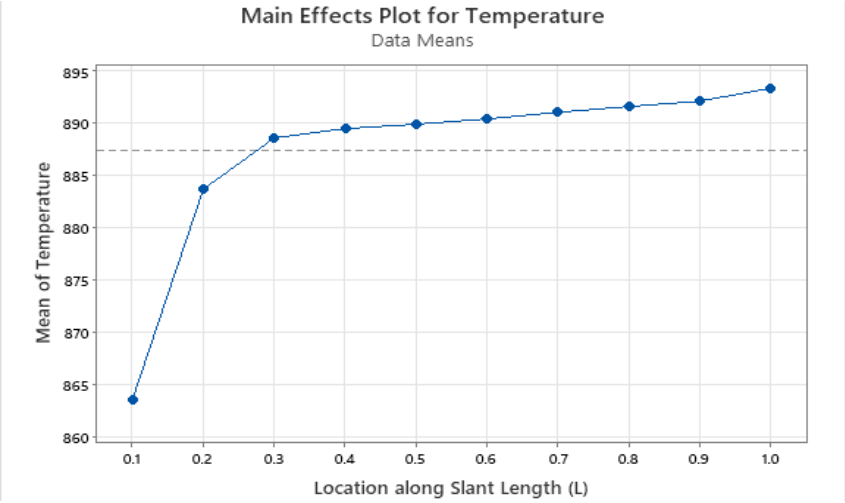


**Fig. 9.** Effect of Location on the static temperature along the slant length of the cone

### *3.4 Interaction Plot of Temperature*

The interaction effects between the semi-cone angle (θ) and the location (x/L) along the slant length of the cone for static temperature are shown in Figure 10. The plot exhibits that temperature increases significantly with increasing Mach number, especially at higher Mach number values. The effect of the semi-cone angle is relatively small for the entire range, but the lines show minor variation across different semi-cone angles of the cone. The location along the slant length doesn't have much impact at lower Mach numbers. Still, it leads to a steady increase in temperature for higher Mach numbers, significantly beyond 0.3 along the slant length. The figure depicts that the Mach number (M) has the most decisive influence on temperature, with higher Mach numbers showing noticeable increases in temperature. The interactions can be comprehended through the fundamental principles of fluid dynamics and thermodynamics, precisely how compressible flow behaves under diverse geometrical constraints. The variations in pressure and temperature correlate with alterations in directional flow and velocity (due to shock waves and boundary layer interactions). However, understanding these principles is essential for interpreting how the aerodynamic design of bodies (such as cones) can influence thermal loads in aerospace applications. That, in turn, impacts material choices and thermal protection systems because the efficiency of these designs can determine performance outcomes. Although the relationships are complex, they underscore the critical nature of these scientific fields in advancing aerospace technology.

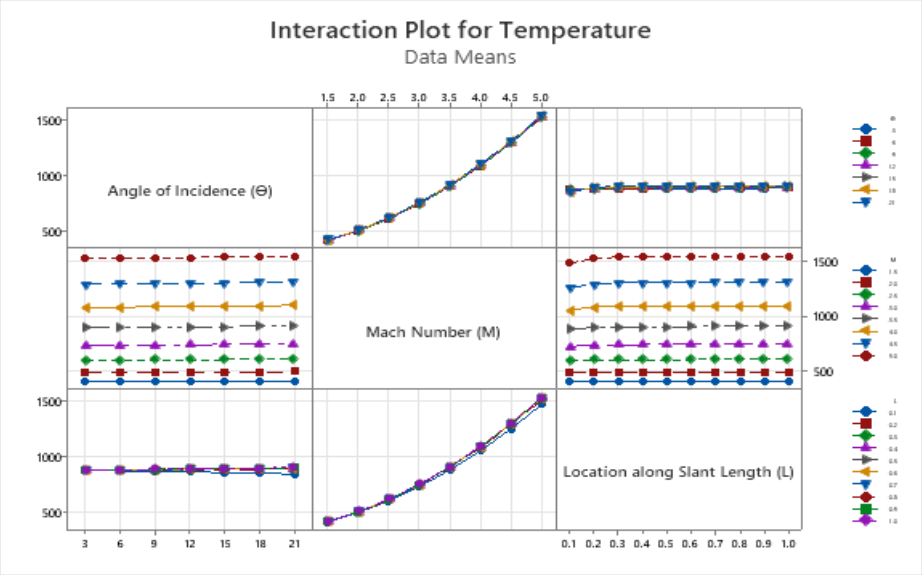


**Fig. 10.** Plot of interaction for static temperature along the slant length cone

### *3.5 Temperature at Various Locations along the Length of the Cone for a Constant Mach Number*

The variation in static temperature at a constant Mach number at the nose of the cone is explored in Figure 11. The figure indicates that for Mach numbers ranging from M = 1.5 to M = 5, there is an apparent stepwise increase in temperature, with each Mach number having a higher temperature than the previous. So, Mach number (M) is the dominant factor affecting temperature, with higher Mach numbers leading to higher temperatures. It is also found that the Semi-cone angle (θ) has a negligible impact on temperature in this range, as temperature remains constant for each Mach number across the angles.

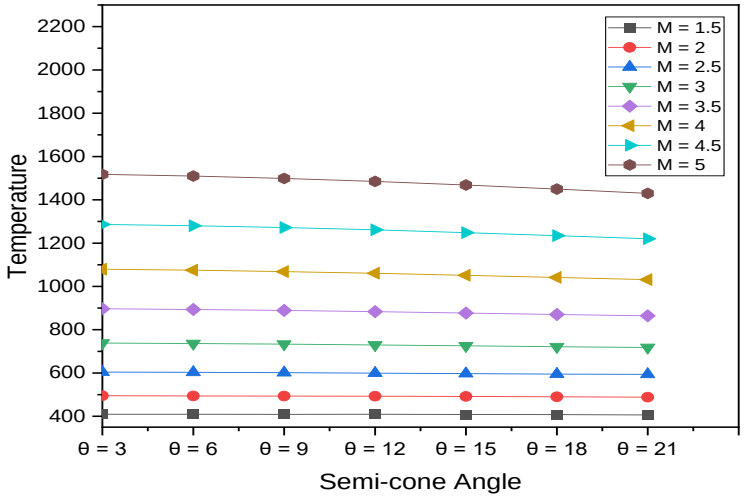


**Fig. 11.** Change in static temperature at the nose of the cone at constant Mach number

### *3.6 Temperature at Various Locations along the Slant Length of the Cone at a Constant Semi-Cone Angle*

The variation in static temperature at a constant semi-cone angle (θ) at the nose of the cone is presented in Figure 12. The figure specifies that the relationship between temperature and Mach

number is approximately exponential, with a sharp rise in temperature beyond Mach 3. Hence, the Mach number is the primary factor influencing temperature, with a clear upward trend as Mach number increases. Semi-cone angle (θ) has a negligible effect on temperature, as indicated by the near-overlap of all the lines for different angles.

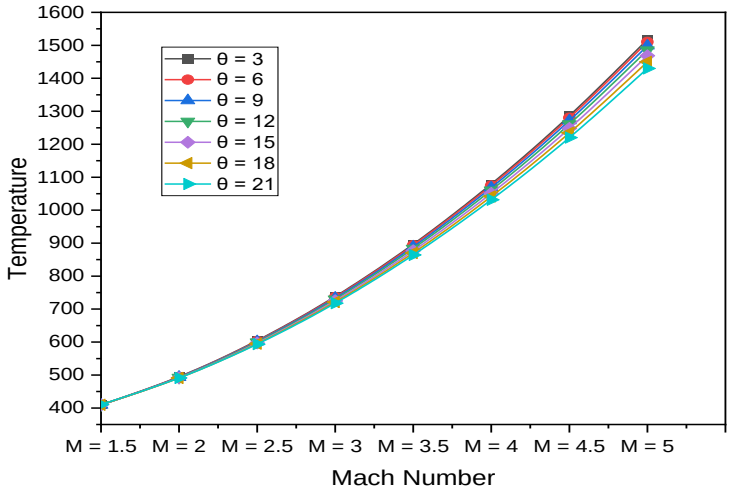


**Fig. 12.** Change in static temperature at the nose of the cone at a constant semi-cone angle

*3.7 The Contour Plot of Temperature Vs. Mach Number and Semi-Cone Angle*

The contour plot for the static temperature vs Mach Number (M) and semi-cone angle (θ) along the slant length of the cone is displayed in Figure 13. It shows the variation in static temperature based on the Mach number (M) and semi-cone angle. The figure shows that the Mach Number is the primary factor influencing temperature, with a significant increase as the Mach number rises. The semi-cone angle (θ) minimizes temperature, as evidenced by the near-vertical color bands.

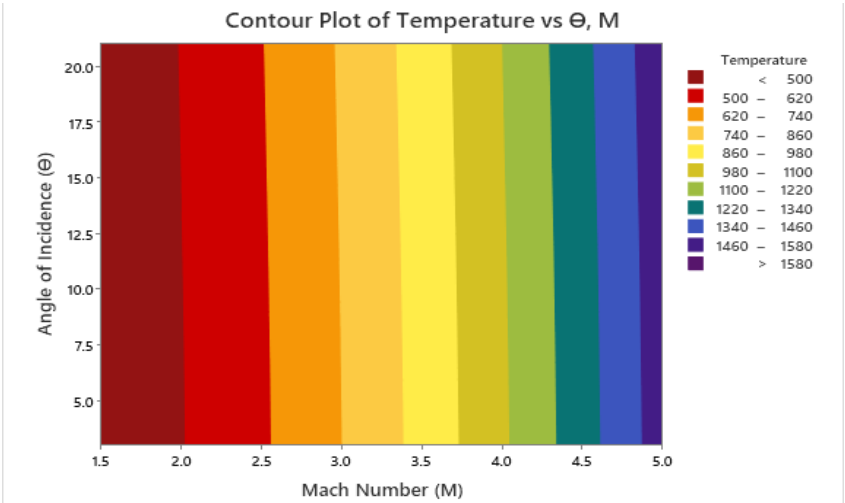


**Fig. 13.** Change in static temperature Vs. Mach number and semi-cone angle along the slant length of the cone

### *3.8 The Contour Plot of Temperature Vs Mach Number and Location along the Slant Length of the Cone Length*

The contour plot for the static temperature vs Mach Number (M) and location along the slant length of the cone is displayed in Figure 14. It shows the variation in static temperature based on the Mach number (M) and location. The figure shows that the contour bands are horizontally aligned, showing that Mach Number significantly impacts temperature, and Location along Slant Length (L) has a minimal impact on temperature, as evidenced by the horizontal color bands.

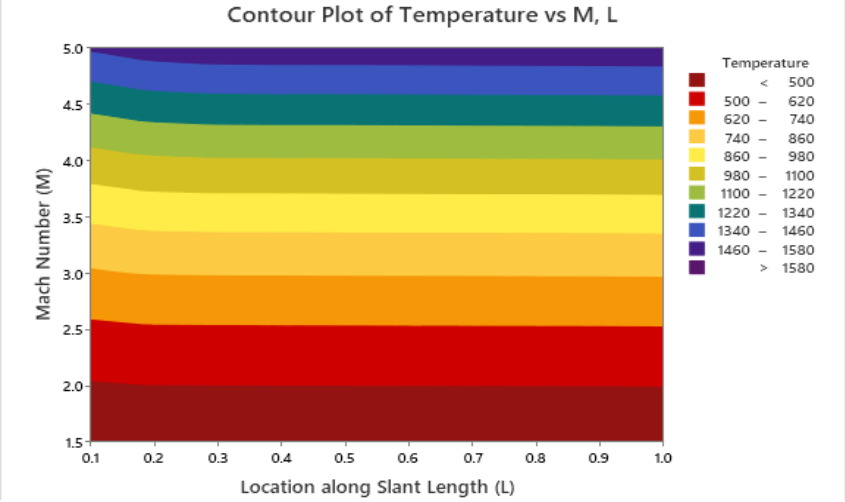


**Fig. 14.** Change in static temperature Vs. Mach number and location along the slant length of the cone

### *3.9 The Contour Plot of Temperature Vs. Semi-cone angle and location along the Cone Slant Length*

The contour plot for the static temperature vs semi-cone angle (θ) and location along the slant length of the cone is displayed in Figure 15. It shows the variation in static temperature based on the semi-cone angle (θ) and location. This contour plot indicates that the semi-cone angle (θ) and the area along the slant length (L) have very little influence on the temperature, which remains relatively constant throughout the plot within a limited temperature range.

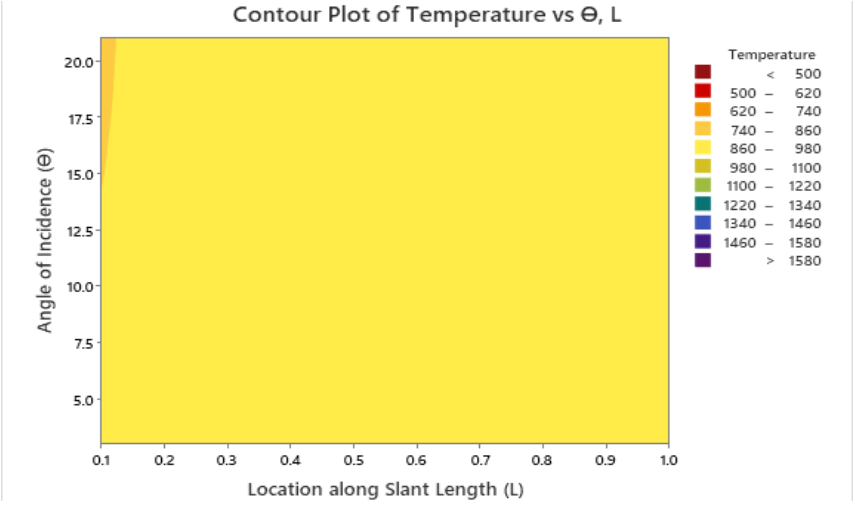


**Fig. 15.** Change in static temperature Vs. semi-cone angle (θ) and location along the slant length of the cone

### *3.10 Regression Analysis for Temperature*

The temperature assessment is done through a regression approach aided by Minitab software. This examination takes into account variables like the semi-cone angle (θ), the Mach number (M), and the position (x/L) along the slant length of the cone. Eq. (4) outlines the regression model to establish the pressure ratio.

$$Temperature = \begin{pmatrix} 299.9 - 0.32\,T + 0.78\,M + 16.7\,L + 0.0018\,T*T - 47.96\,M*M - 169.6\,L*L \\ - 0.558\,T*M + 5.29\,T*L + 21.13\,M*L - 0.047\,M*M*M - 0.00040\,T*T*T \\ + 188.9\,L*L*L - 0.0035\,M*M*T + 2.453\,M*M*L + 0.00721\,M*T*T \\ + 0.0149\,L*T*T + 2.453\,M*L*L - 6.963\,T*L*L + 1.193\,M*T*L \end{pmatrix} \quad (4)$$

### *3.11 Regression Model Summary*

Table 2 provides an overview of the regression analysis conducted to investigate the relationship between Mach number (M), semi-cone angle (θ), and position (x/L). In this research, the adjusted $R^{2,}$ a statistical metric, is employed to assess the accuracy of the regression model in representing the temperature at supersonic velocities. This metric indicates the extent to which the independent variables can explain variations in the variable. The high adjusted $R^2$ value of 96.21% means that the model successfully captures the relationship between the independent variables and the temperature.

**Table 2**
Summary of Regression model

| S | R-square | R-square(adj) | R-square(pred) |
|---|---|---|---|
| 5.85121 | 96.27% | 96.15% | 96.21% |

## 4. Results for Pressure

### *4.1 Main Effects Mach Number Plots for Dimensionless Static Pressure*

The main effects plot illustrated in Figure 16 showcases the relationship between the Mach Number (M) and the average pressure ratio (P/Pa). It shows a positive, non-linear relationship between the Mach number (M) and the pressure ratio (P/Pa). Specifically, it indicates that the pressure ratio gradually increases as the Mach number falls between 1.5 to 2.5. However, once the Mach number surpasses 3.0, the curve becomes steeper, signifying a more significant rise in the pressure ratio.

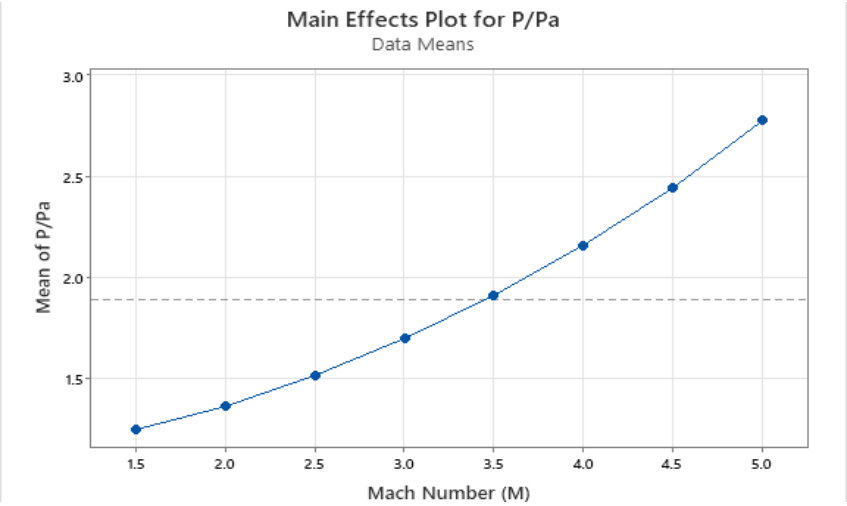


**Fig. 16.** Effect of Mach numbers on the pressure ratio along the slant length of the cone

### *4.2 Main Effects Semi-Cone Angle Plots for Dimensionless Static Pressure*

The main effects plot illustrated in Figure 17 showcases the relationship between the semi-cone angle (θ) and the average pressure ratio (P/Pa). It shows a positive, non-linear relationship between the semi-cone angle (θ) and the average pressure ratio (P/Pa). Figure 3 indicates that the pressure ratio gradually increases for the lower semi-cone angle of incidence fall between 3° and 9°. Moreover, the curve becomes steeper, signifying a more significant rise in the pressure ratio for the semi-cone angle, which ranges between 12° and 21°.

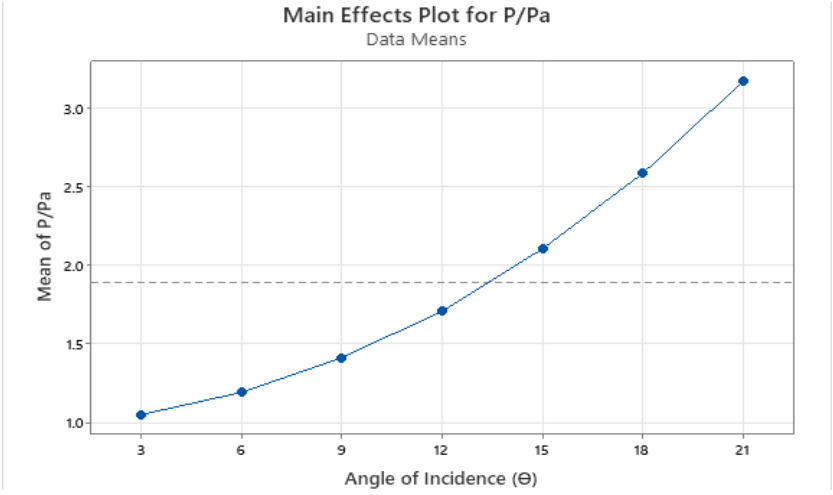


**Fig.17.** Effect of semi-cone angle on the pressure ratio along the slant length of the cone

### *4.3 Main Effects of Location along Slant Length of the Cone for Dimensionless Static Pressure*

Figure 18 shows the main effect of location (x/L) along the slant length of the cone plots for dimensionless static pressure. This main effects plot shows the relationship between the location (x/L) along the slant length (L) and the mean of the pressure ratio (P/Pa). The diagram indicates that the pressure ratio increases sharply along the slant length, reaching a peak at L=0.3. After a slight drop, it stabilizes and rises again toward the end of the slant length. The plot shows some fluctuations

in the pressure ratio after the initial peak at L=0.3, but overall, the values stabilize near 2.0 along the slant length. This behavior may be attributed to variations in aerodynamic pressure distribution along the length of the surface.

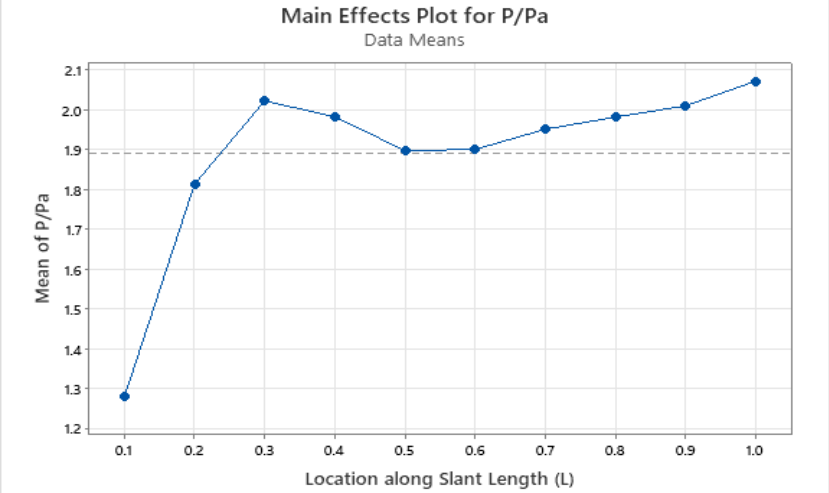


**Fig. 18.** Main effect of location on the pressure ratio along the slant length of the cone

### *4.4 Interaction Plot Among the Parameter Mach Number (M), Semi-Cone Angle (Θ), and Location (X/L) for Surface Pressure Distribution Along the Slant Length of the Cone*

Figure 19 displays the interaction plot among the parameter Mach number (M), semi-cone angle (θ), and the location (x/L) along the slant length of the cone for dimensionless static pressure. This plot shows the variation in surface pressure with the factors Mach number (M), semi-cone angle (θ), and the location (x/L) along the slant length of the cone. The pressure ratio remains low across different semi-cone angles for lower Mach numbers (M = 1.5). In contrast, as the Mach number increases, the pressure ratio rises significantly, especially at higher angles of incidence. The diagram indicates that at higher Mach numbers, there is a noticeable increase in pressure ratio as the location along the slant length progresses. It is also observed that as the semi-cone angle increases, the pressure ratio rises as the location along the slant length exceeds. So, it shows that higher Mach numbers, larger semi-cone angles, and increased location along the slant length all lead to higher pressure ratios, with stronger interactions observed at higher values of these parameters.

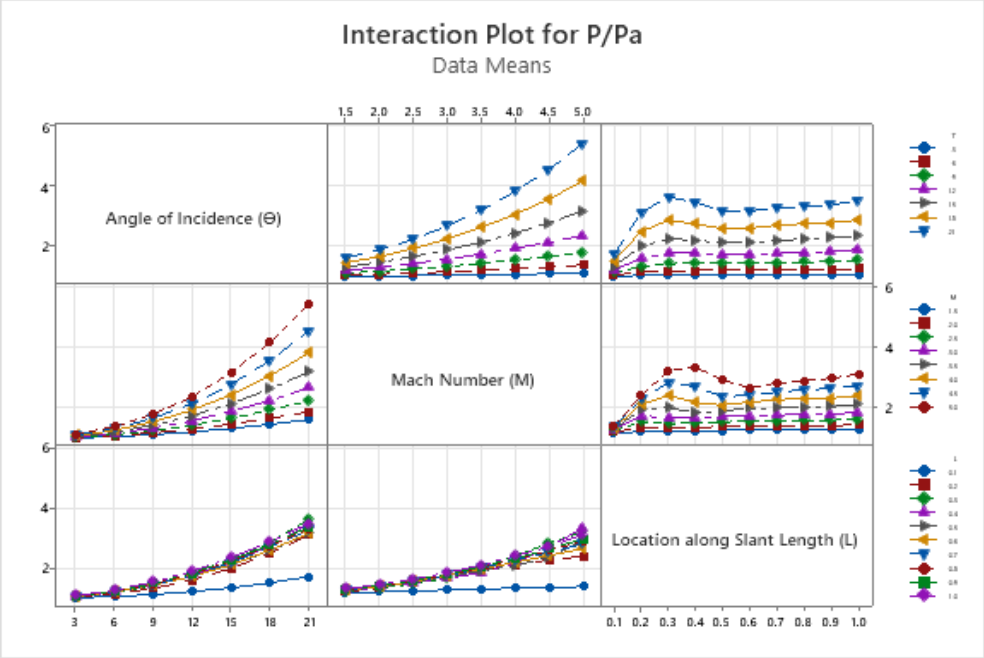


**Fig. 19.** Plot of interaction for pressure ratio along the slant length cone

*4.5 Surface Pressure at Various Locations along the Length of the Cone for a Constant Mach Number*

From the ANSYS software, the CFD analysis yielded pressure results at different locations along the cone's slant length (x/L), with a constant Mach number. The non-dimensional pressure values are calculated by dividing the static pressure by atmospheric pressure.

The variation in dimensionless static pressure ratio (P/Pa) vs (x/L) ratio along the slant length of the cone for different semi-cone angles (θ) at constant Mach numbers from M = 1.5 to M = 5 are displayed in the Figures 20(a) to 20(h). These figures show a continuous rise in the pressure as the semi-cone angle increases at each location. The pressure ratio rises at the location (x/L) = 0.1 for each semi-cone angle. It is observed that the pressure ratio remains relatively low and almost constant across the length for lower semi-cone angles. In comparison, the marginal change in pressure is observed at the location for higher semi-cone angles. The figures demonstrate that for the Mach numbers from M=2, 2.5, and 3, the pressure increases till the location 0.2 and then falls at the location 0.3. Once location 0.3 surpasses the pressure ratio, it rises until location 0.5, and then marginal variation is seen in the pressure ratio from location 0.5 to 1.0.

Similarly, for the Mach numbers M = 4 and 4.5, the pressure ratio rises to location 0.3. Then, it falls from location 0.3, with minimal variation pressure ratio distributed till up to location 1. At Mach number M = 5, the pressure ratio overgrows up to location 0.4 and falls until location 0.6. After location 0.6, the pressure ratio increases with minimal variation until location 1.0. These figures depict that the fluctuation in pressure ratio is significant for high Mach numbers and large semi-cone angles.

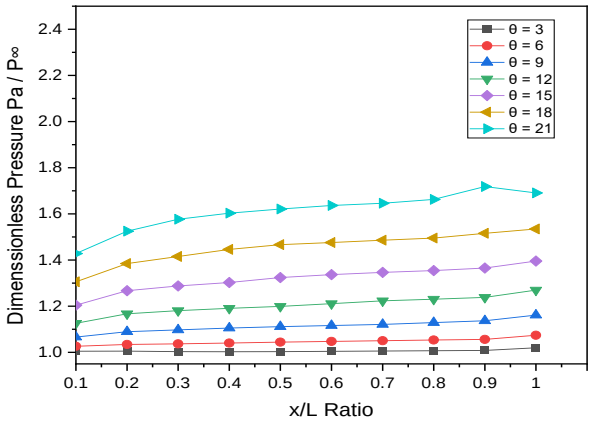


**Fig. 20(a).** Change dimensionless pressure along the slant length (x/L) at M = 1.5

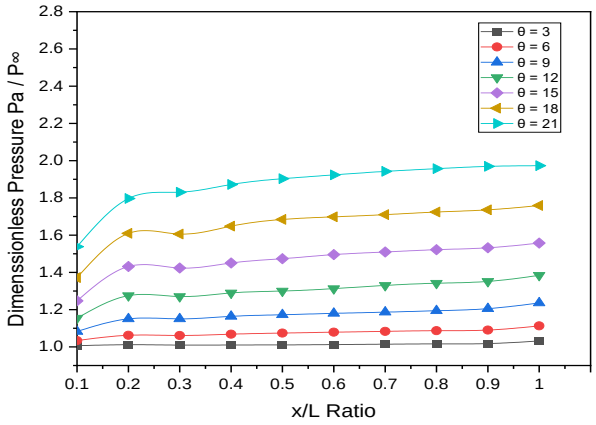


**Fig. 20(b).** Change dimensionless pressure along the slant length (x/L) at M = 2

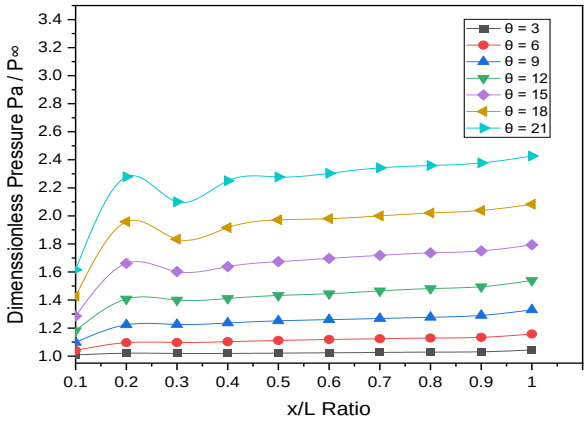


**Fig. 20(c).** Change dimensionless pressure along the slant length (x/L) at M = 2.5

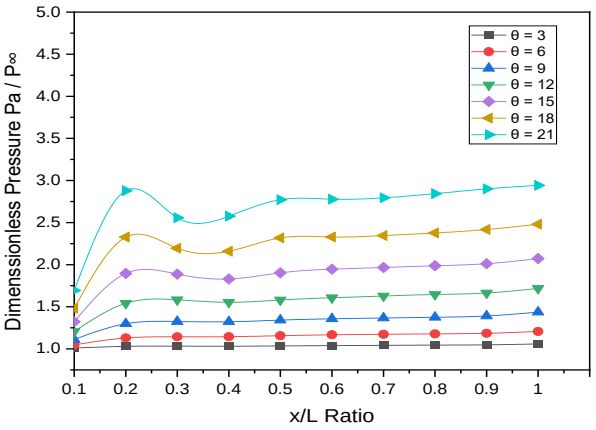


**Fig. 20(d).** Change dimensionless pressure along the slant length (x/L) at M = 3

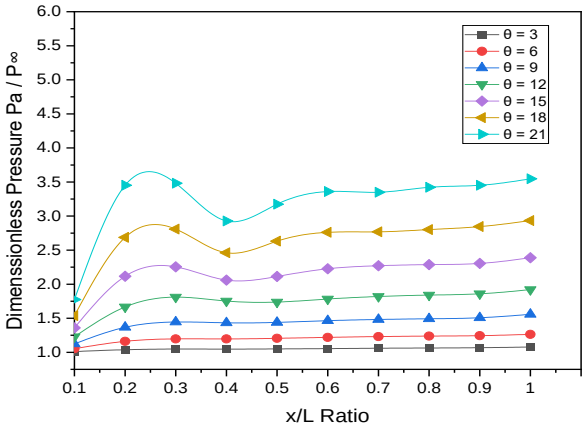


**Fig. 20(e).** Change dimensionless pressure along the slant length (x/L) at M = 3.5

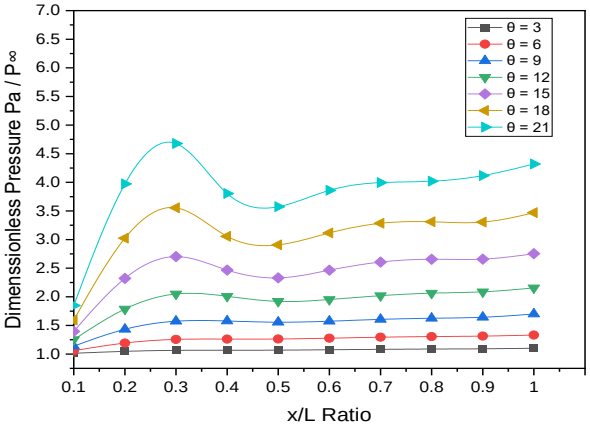


**Fig. 20(f).** Change dimensionless pressure along the slant length (x/L) at M = 4

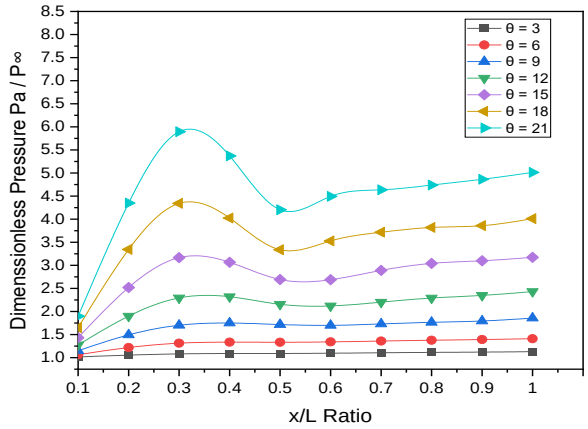


**Fig. 20(g).** Change dimensionless pressure along the slant length (x/L) at M = 4.5

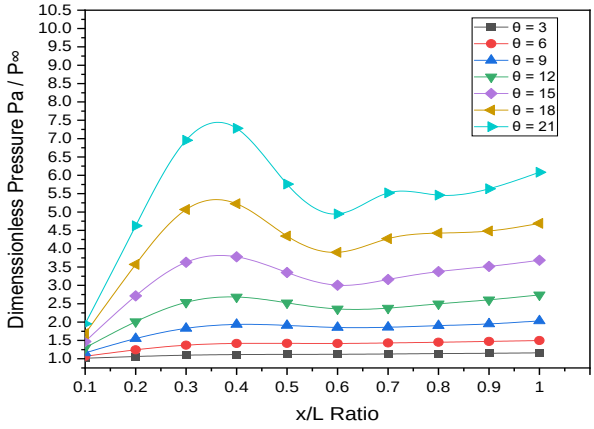


**Fig. 20(h).** Change dimensionless pressure along the slant length (x/L) at M = 5

### *4.6 Surface Pressure at Various Locations along the Slant Length of the Cone at a Constant Semi-Cone Angle*

From the ANSYS software, the CFD analysis yielded pressure results at different positions along the cone's slant length (x/L) with a consistent semi-cone angle. The non-dimensional pressure values are calculated by dividing the static pressure by atmospheric pressure.

The variation in dimensionless static pressure ratio (P/Pa) Vs. (x/L) ratio along the slant length of the cone for different Mach numbers from at a constant semi-cone angle (θ) are displayed in the figures from 21(a) to 21(g). The figures showcased a continuous rise in pressure ratio as the Mach number increased at each location. Figures 21(a) to 21(c) show that the pressure grows up to location 0.4, and a minimal variation is observed from 0.4 onwards to 1. It was also found that the fluctuation in pressure ratio is significant for higher Mach numbers and large semi-cone angles.

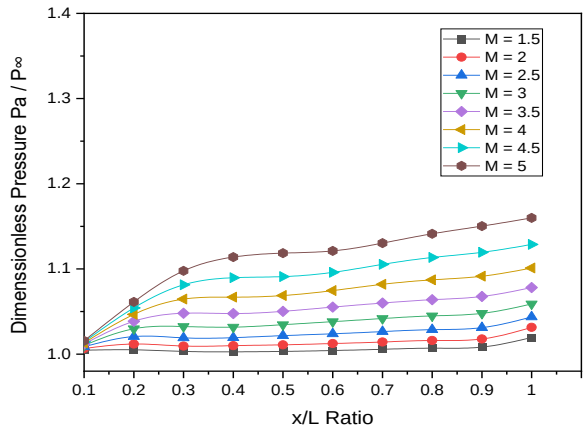


**Fig. 21(a).** Change dimensionless pressure along the slant length (x/L) at θ = 3°

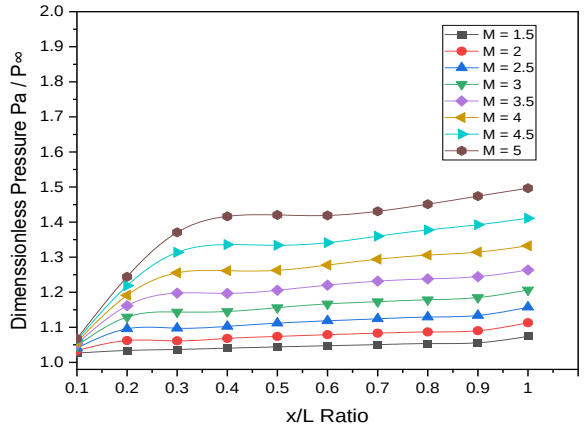


**Fig. 21(b).** Change dimensionless pressure along the slant length (x/L) at θ = 6°

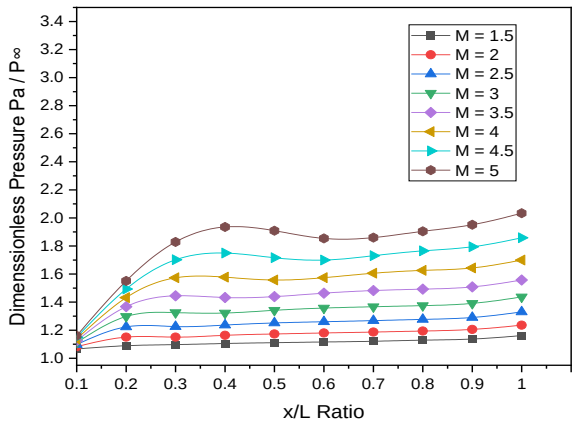


**Fig. 21(c).** Change dimensionless pressure along the slant length (x/L) at θ = 9°

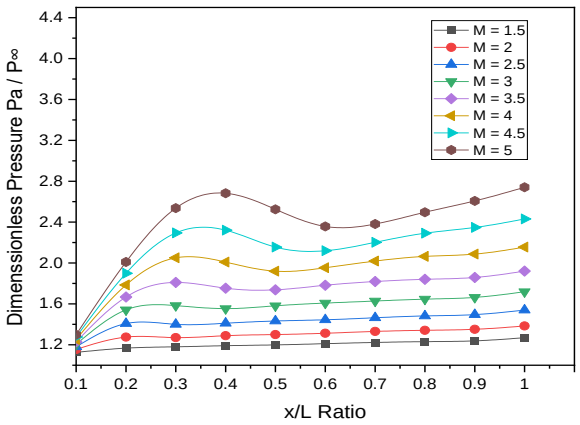


**Fig. 21(d).** Change dimensionless pressure along the slant length (x/L) at θ = 12°

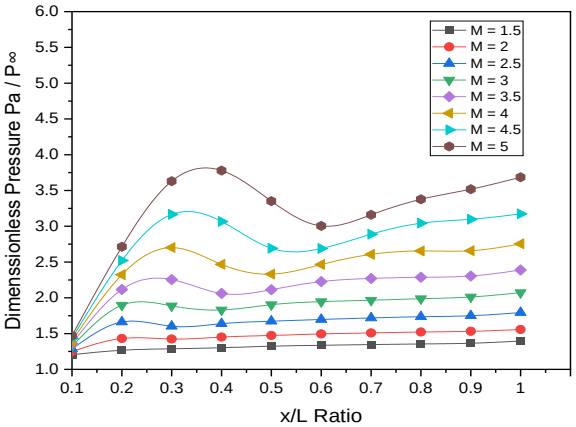


**Fig. 21(e).** Change dimensionless pressure along the slant length (x/L) at θ = 15°

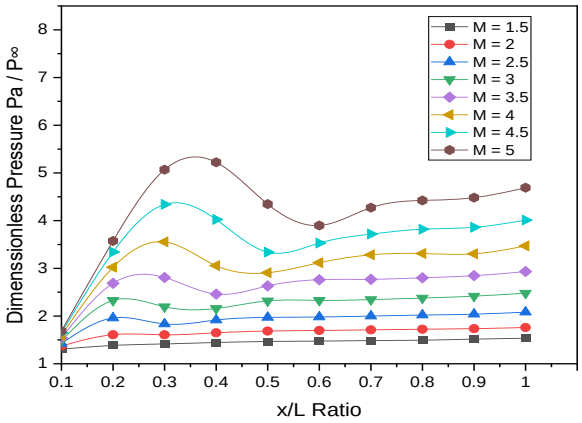


**Fig. 21(f).** Change dimensionless pressure along the slant length (x/L) at θ = 18°

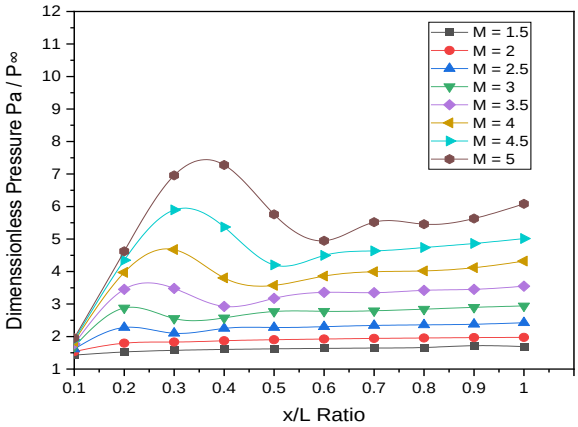


**Fig. 21(g).** Change dimensionless pressure along the slant length (x/L) at θ = 21°

### *4.7 The Contour Plot of Dimensionless Pressure Vs Mach Number and Semi-Cone Angle*

The contour plot for the pressure ratio (P/Pa) vs Mach Number (M) and semi-cone angle (θ) along the slant length of the cone is displayed in Figure 22. It shows how the dimensionless pressure ratio (P/Pa) varies based on the Mach number (M) and the semi-cone angle (θ). The plot demonstrates a

strong interaction between Mach number and angle of incidence in influencing the pressure ratio (P/Pa). The highest pressure ratios are achieved at large angles of incidence combined with high Mach numbers, which is expected in supersonic and hypersonic aerodynamic regimes.

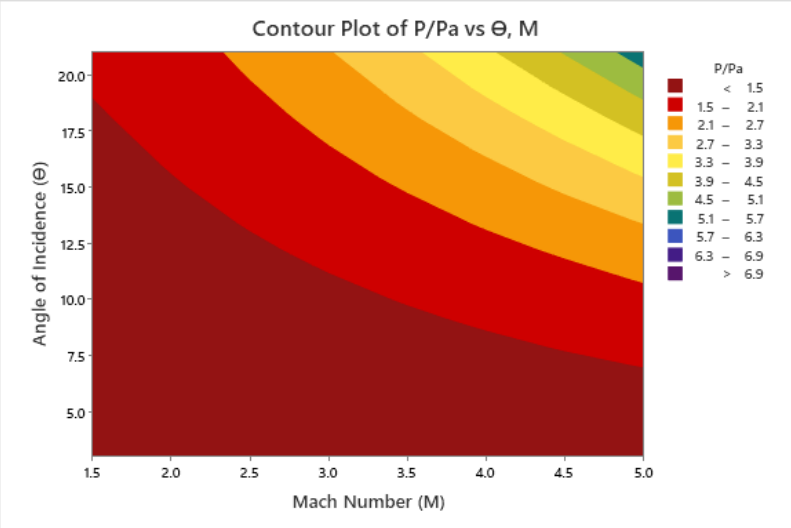


**Fig. 22.** Change in pressure ratio Vs. Mach number and semi-cone angle along the slant length of the cone

*4.8 The Contour Plot of Dimensionless Pressure Vs Mach Number and Location along the Slant Length of the Cone Length*

The contour plot for the pressure ratio (P/Pa) vs Mach Number (M) and the Location along the slant length of the cone is displayed in Figure 23. It shows the dimensionless pressure ratio (P/Pa) based on the Mach number (M) and the location. The plot illustrates the dependence of the dimensionless pressure ratio (P/Pa) on the Mach number and the area along the slant length of the surface. Higher Mach numbers (beyond Mach 4) lead to higher pressure ratios, while the position along the slant length shows that the highest pressures occur near the start of the slant length.

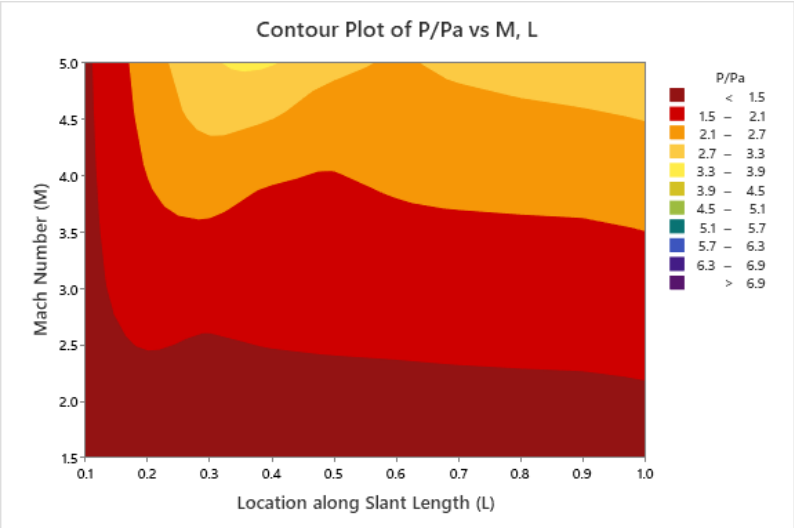


**Fig. 23.** Change in pressure ratio Vs. Mach number and location along the slant length of the cone

### *4.9 The Contour Plot of Dimensionless Pressure Vs. Semi-cone angle and location along the Slant Length of the Cone Length*

The contour plot for the pressure ratio (P/Pa) vs semi-cone angle (θ) and the location along the slant length of the cone is displayed in Figure 24. It shows the variation in dimensionless pressure ratio (P/Pa) based on the semi-cone angle (θ) and the location. The contour plot indicates that both the angle of incidence and the slant length significantly influence the pressure distribution across the surface. Higher incidence and slant length angles lead to a more excellent dimensionless pressure ratio (P/Pa), especially in angles above 15°.

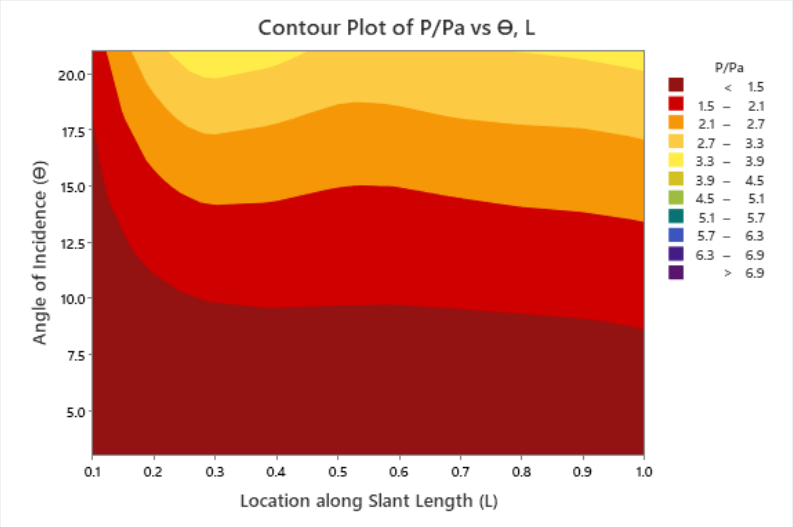


**Fig. 24.** Change in pressure ratio Vs. semi-cone angle and location along the slant length of the cone

### *4.10 Regression Analysis for Pressure*

The evaluation of the pressure ratio is conducted using a regression method with the assistance of Minitab software. This analysis considers factors such as the semi-cone angle (θ), the Mach number (M), and the location along the slant length of the cone. The regression framework used to determine the pressure ratio is described in Eq. (5).

$$P/P_a = \begin{pmatrix} 0.352 + 0.118\,T + 0.413\,M + 1.224\,L - 0.00527\,T*T - 0.099\,M*M - 6.88\,L*L \\ -0.0866\,T*M + 0.1489\,T*L + 0.703\,M*L + 0.0028\,M*M*M + 0.000035\,T*T*T \\ +6.372\,L*L*L + 0.01009\,M*M*T + 0.0336\,M*M*L + 0.002707\,M*T*T + 0.00023\,L*T*T \\ -0.881\,M*L*L - 0.1659\,T*L*L + 0.02452\,M*T*L \end{pmatrix} \quad (5)$$

### *4.11 Regression Model Summary*

Table 3 presents a summary of the regression analysis used to explore the connection between Mach number (M), semi-cone angle (θ), and location (x/L). In this study, the adjusted $R^2$ is a statistical indicator to evaluate how well the regression model portrays the dimensionless static pressure ratio at supersonic speeds. This measure indicates how much of the variation in the dependent variable can be accounted for by the independent variables. With an $R^2$ score of 93.85%, this study suggests that the regression model successfully reflects the data trends.

**Table 3**
Summary of regression model

| S | R-square | R-square(adj) | R-square(pred) |
|---|---|---|---|
| 0.256843 | 94.07% | 93.85% | 93.23% |

## 5. Validation of CFD and Regression Results for Temperature and Pressure Ratio

Figures 25(a) and 25(b) compare the results obtained from CFD analysis and those derived through regression methods. These visuals illustrate the relationship between variation in temperature and pressure ratio at a semi-cone angle of θ = 12° for the Mach number ranging from M = 1.5 to 5 at the constant location (x/L) = 0.6 along the slant length of the cone using both CFD and regression approaches. The images presented in Figures 25(a) and 25(b) reveal a consistency between the findings of the CFD analysis and the regression method analysis regarding variation in static temperature and pressure ratio. The regression model will be helpful in the case of an attached shock wave.

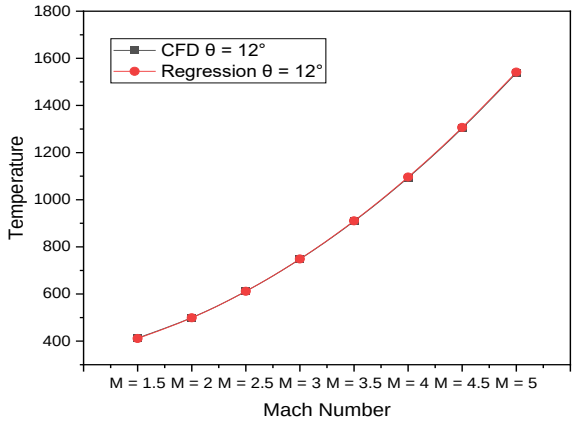


**Fig. 25(a).** Comparison of Variation of temperature by CFD and by regression method at θ = 12°

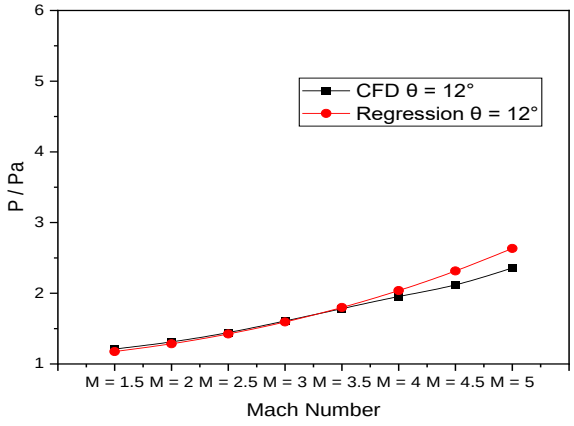


**Fig. 25(b).** Comparison of Variation of pressure ratio by the CFD and by regression method at θ = 12°

## 6. Conclusions

The research showcases the versatility of its applications in defense and aerospace sectors, focusing on factors such as Mach number, semi-cone angle, and cone slant length. The findings reveal a notable increase in temperature with rising Mach number, particularly in higher Mach number ranges. The impact of the semi-cone angle on static temperature variation along the cone slant length is relatively minimal. The Mach number, semi-cone angle, and location play significant roles in static pressure variation. The pressure ratio remains low across various semi-cone angles for lower Mach numbers while it significantly increases with the Mach number, particularly at higher semi-cone angles. Higher Mach numbers, larger semi-cone angles, and increased locations along the slant length of the cone all contribute to higher pressure ratios. The outcomes from the CFD analysis and regression methods show an excellent agreement. This study yields results with notable computational efficiency. These discoveries prove valuable during the design phase of aerospace vehicles due to the high costs associated with wind tunnel testing. Therefore, these findings can be utilized in the initial development stages to enhance the design of aerospace vehicles.

## Acknowledgment
The authors received no specific funding for this study.

## References
[1] Tsien, Hsue-shen. "Similarity laws of hypersonic flows." *Collected Works of HS Tsien (1938-956)* (1946): 443-447. https:// doi.org.10.1002/sapm1946251247
[2] Hayes, Wallace D. "On hypersonic similitude." *Quarterly of Applied Mathematics* 5, no. 1 (1947): 105-106. https://doi.org/10.1090/qam/ 20904
[3] Sychev, V. V, "Three Dimensional Hypersonic Gas Flow Past Slender Bodies at High Angles of Attack." *Journal of Applied Mathematics and Mechanics* 24, no.2 (1960): 205-212. https://doi.org/10.1016/0021-8928(60)90033-2
[4] Pike. J, "The pressure on flat and anhydral delta wings with attached shock waves." *The Aeronautical Quarterly* 23, no.4 (1972): 253-262. https://doi.org/10.1017/S0001925900006156
[5] Hui, Wai How. "Stability of oscillating wedges and caret wings in hypersonic and supersonic flows." *AIAA Journal* 7, no. 8 (1969): 1524-1530. https://doi.org/10.2514/3.5426
[6] Carrier, G. F. "The oscillating wedge in the supersonic stream." *Journal of Aeronautical Sciences* 16, no. 3 (1949): 150–152. https:// doi.org.10.2514/8.11755
[7] Hui, W. H. "Supersonic/hypersonic flow past on oscillating flat plate at high angles of attack." *ZAMP* 29, (1978): 414-427. https://doi.org/10.1007/BF01590763
[8] Orlik-Ruckemann, K. J. "Dynamic stability testing of aircraft needs versus capabilities." *Progress in the Aerospace Sciences, Academic press* 16, (1975): 431-447. https://doi.org/10.1016/0376-0421(75)90005-6
[9] Liu, D. D., and W. H. Hui. "Oscillating delta wings with attached shock waves." *AIAA Journal* 15, no. 6 (1977): 804-812. https://doi.org/10.2514/3.7371
[10] Hui, W. H., Hemdan, H. T. "Unsteady hypersonic flow over delta wings with detached shock waves." *American Institute of Aeronautics and Astronautics Journal* 14, no. 4 (1976): 505–511. https://doi.org.10.2514/3.7120
[11] Lighthill, Mo J. "Oscillating airfoils at high Mach number." *Journal of the Aeronautical Sciences* 20, no. 6 (1953): 402-406. https://doi.org/10.2514/8.2657
[12] Ghosh, K. "A new similitude for aerofoils in hypersonic flow." In *Proceedings of the 6th Canadian Congress of Applied Mechanics, Vancouver, Canada, May*, pp. 685-686. 1977.
[13] Miles, J. W. "Unsteady flow at hypersonic speeds, Hypersonic flow." *Butter worths Scientific Publications, London* (1960): 185-197.
[14] Ghosh, Kunal, and Binoy Krishna Mistry. "Large incidence hypersonic similitude and oscillating nonplanar wedges." *AIAA Journal* 18, no. 8 (1980): 1004-1006. https://doi.org/10.2514/3.7702
[15] Ghosh, Kunal. "Hypersonic large-deflection similitude for quasi-wedges and quasi-cones." *The Aeronautical Journal* 88, no. 873 (1984): 70-76. https://doi.org/10.1017/S0001924000020236
[16] Khan, Sher Afghan, Abdul Aabid, and C. Ahamed Saleel. "CFD simulation with analytical and theoretical validation of different flow parameters for the wedge at supersonic Mach number." *International Journal of Mechanical and Mechatronics Engineering* 1 (2019). https://www.researchgate.net/publication/331556786
[17] Bashir, Musavir, S. A. Khan, Qummare Azam, and Ayub Ahmed Janvekar. "Computational and Analytical Investigation of Aerodynamic Derivatives of Similitude Delta Wing Model at Hypersonic Speeds." *International Journal of Technology* 8, no. 3 (2017). https://doi.org.10.14716/ijtech.v8i3.6319
[18] Kalimuthu, R., R. C. Mehta, and E. Rathakrishnan. "Measured aerodynamic coefficients of without and with spiked blunt body at Mach 6." *Journal of the Korean Society of Propulsion Engineers* 25, no. 1 (2019): 29-41. https://doi.org/10.12989/aas.2019.6.3.225
[19] Pathan, Khizar A., Sher A. Khan, N. A. Shaikh, Arsalan A. Pathan, and Shahnawaz A. Khan. "An investigation of boattail helmet to reduce drag." *Advances in Aircraft and Spacecraft Science* 8, no. 3 (2021): 239. https://doi.org/10.12989/aas.2021.8.3.239
[20] Shaikh Javed, Kumar Krishna, Pathan Khizar, and Khan Sher. "Analytical and computational analysis of pressure at the nose of a 2D wedge in high-speed flow." *Advances in Aircraft and Spacecraft Science* 9, no. 2 (2022): 119-130. https://doi.org/10.12989/aas.2022.9.2.119
[21] Shaikh, Javed S., Krishna Kumar, Khizar A. Pathan, and Sher A. Khan. "Computational analysis of surface pressure distribution over a 2d wedge in the supersonic and hypersonic flow regimes." *Fluid Dynamics & Materials Processing* 19, no. 6 (2023). https://doi.org/10.32604/fdmp.2023.025113
[22] Shaikh, Javed Shoukat, Khizar Ahmed Pathan, Krishna Kumar, and Sher Afghan Khan. "Effectiveness of Cone Angle on Surface Pressure Distribution along Slant Length of a Cone at Hypersonic Mach Numbers." *Journal of Advanced Research in Fluid Mechanics and Thermal Sciences* 104, no. 1 (2023): 185-203. https://doi.org/10.37934/arfmts.104.1.185203

[23] Azami, Muhammed Hanafi, Mohammed Faheem, Abdul Aabid, Imran Mokashi, and Sher Afghan Khan. "Experimental research of wall pressure distribution and effect of micro jet at Mach." *International Journal of Recent Technology and Engineering* 8, no. 2S3 (2019): 1000-1003. https://doi.org. 10.35940/ijrte.B1187.0782S319
[24] Pathan, Khizar Ahmed, Prakash S. Dabeer, and Sher Afghan Khan. "Investigation of base pressure variations in internal and external suddenly expanded flows using CFD analysis." *CFD Letters* 11, no. 4 (2019): 32-40.
[25] Khan, Sher Afghan, and E. Rathakrishnan. "Active control of base pressure in supersonic regime." *Journal of Aerospace Engineering, Institution of Engineers, India* 87 (2006): 1-8.
[26] Pathan, Khizar, Prakash Dabeer, and Sher Khan. "An investigation of effect of control jets location and blowing pressure ratio to control base pressure in suddenly expanded flows." *Journal of Thermal Engineering* 6, no. 2 (2019): 15-23. https://doi.org/10.18186/thermal.726106
[27] Pathan, Khizar Ahmed, Syed Ashfaq, Prakash S. Dabeer, and Sher Afgan Khan. "Analysis of parameters affecting thrust and base pressure in suddenly expanded flow from nozzle." (2019).
[28] Pathan, Khizar Ahmed, Prakash S. Dabeer, and Sher Afghan Khan. "Influence of expansion level on base pressure and reattachment length." *CFD Letters* 11, no. 5 (2019): 22-36.
[29] Pathan, Khizar Ahmed, Prakash S. Dabeer, and Sher Afghan Khan. "Effect of nozzle pressure ratio and control jets location to control base pressure in suddenly expanded flows." *Journal of Applied Fluid Mechanics* 12, no. 4 (2019): 1127-1135. https://doi.org/10.29252/jafm.13.02.30049
[30] Pathan, Khizar Ahmed, Prakash S. Dabeer, and Sher Afghan Khan. "Enlarge duct length optimization for suddenly expanded flows." *Advances in Aircraft Spacecraft and spacecraft Science* 7, no. 3 (2020): 203–214. https://doi.org/10.12989/aas.2020.7.3.203
[31] Pratibha V. Jadhav, Vaishali Patil, Sharad Gore. "A Comparative Study of Linear Regression and Regression Tree." *2nd International Conference on Communication and Information Processing* (ICCIP-2020). https://dx.doi.org/10.2139/ssrn.3645883
[32] Pratibha V. Jadhav, Vaishali Patil, Sharad Gore. "Classification of Categorical Outcome Variable Based on Logistic Regression and Tree Algorithm." *International Journal of Recent Technology and Engineering* 8, no. 5 (2020): 4685-4690. https://dx.doi.org/10.35940/ijrte.E6844.018520
[33] Aqilah, Nur, Khizar Ahmed Pathan, and Sher Afghan Khan. "Passive Control of Base Flow at Supersonic Mach Number for Area Ratio 4." In *International Conference on Advances in heat Transfer and Fluid Dynamics*, pp. 37-50. Singapore: Springer Nature Singapore, 2022. https://doi.org/10.1007/978-981-99-7213-5_4
[34] Fiqri, Muhammad Ikhwan, Khizar Ahmed Pathan, and Sher Afghan Khan. "Control of Suddenly Expanded Flow with Cavity at Sonic Mach Number." In *International Conference on Advances in heat Transfer and Fluid Dynamics*, pp. 3-15. Singapore: Springer Nature Singapore, 2022. https://doi.org/10.1007/978-981-99-7213-5_1
[35] Pathan, Khizar Ahmed, Zakir Ilahi Chaudhary, Ajaj Rashid Attar, Sher Afghan Khan, and Ambareen Khan. "Optimization of Nozzle Design for Weight Reduction using Variable Wall Thickness." *Journal of Advanced Research in Fluid Mechanics and Thermal Sciences* 112, no. 2 (2023): 86-101. https://doi.org/10.37934/arfmts.112.2.86101
[36] Shaikh, Sohel Khalil, Khizar Ahmed Pathan, Zakir Ilahi Chaudhary, B. G. Marlpalle, and Sher Afghan Khan. "An investigation of three-way catalytic converter for various inlet cone angles using CFD." *CFD Letters* 12, no. 9 (2020): 76-90. https://doi.org/10.37934/cfdl.12.9.7690
[37] Shaikh, Sohel Khalil, Khizar Ahmed Pathan, Zakir Ilahi Chaudhary, and Sher Afghan Khan. "CFD Analysis of an Automobile Catalytic Converter to Obtain Flow Uniformity and to Minimize Pressure Drop Across the Monolith." *CFD Letters* 12, no. 9 (2020): 116-128. https://doi.org/10.37934/cfdl.12.9.116128
[38] Kumar, Pankaj, and Jiten C. Kalita. "A transformation-free ψ-v formulation of the Navier–Stokes equations on compact nonuniform grids." *Journal of Computational and Applied Mathematics* 353 (2019): 292-317. https://doi.org/10.1016/j.cam.2018.12.035
[39] Kumar, Pankaj, and Jiten C. Kalita. "An efficient ψ-v scheme for two-dimensional laminar flow past bluff bodies on compact nonuniform grids." *International Journal for Numerical Methods in Fluids* 92, no. 12 (2020): 1723-1752. https://doi.org/10.1002/fld.4846
[40] Kalita, Jiten C., and Pankaj Kumar. "Vortex dynamics of accelerated flow past a mounted wedge." *Physics of Fluids* 35, no. 12 (2023). https://doi.org/10.1063/5.0177161
[41] Akbar, Noreen Sher, Javaria Akram, M. Fiaz Hussain, E. N. Maraj, and Taseer Muhammad. "Thermal storage study and enhancement of heat transfer through hybrid Jeffrey nanofluid flow in ducts under peristaltic motion with entropy generation." *Thermal Science and Engineering Progress* 49 (2024): 102463. https://doi.org/10.1016/j.tsep.2024.102463
[42] Akbar, Noreen Sher, Tayyab Zamir, and Taseer Muhammad. "Levenberg-Marquardt technique analysis of thermal and concentration storage in cone-disk apparatus with neural network-enhancement." *Thermal Science and Engineering Progress* 50 (2024): 102529. https://doi.org/10.1016/j.tsep.2024.102529

[43] Akbar, Noreen Sher, Tayyab Zamir, Javaria Akram, Tayyaba Noor, and Taseer Muhammad. "Simulation of hybrid boiling nano fluid flow with convective boundary conditions through a porous stretching sheet through Levenberg Marquardt artificial neural networks approach." *International Journal of Heat and Mass Transfer* 228 (2024): 125615. https://doi.org/10.1016/j.ijheatmasstransfer.2024.125615